Synergistic modification of bentonite by acid activation and hydroxyl iron pillaring for enhanced dye adsorption capacity

Huan Xi, Qingqing Li, Yan Yang, Jianfeng Zhang, Feng Guo, Xiaogang Wang, Shikai Xu and Shiping Ruan

ABSTRACT

Despite the fact of natural abundance, low cost and environmental friendliness, the far-from-sufficient adsorption capacity of natural bentonite (BT) has limited such a promising application to remove dye pollutants. In this paper, we proposed a facile modification strategy to enhance adsorption performance of bentonite utilizing synergistic acid activation and hydroxyl iron pillaring, by which the adsorbent (abbreviated as S-Fe-BT) exhibited the highest adsorption capacity (246.06 mg/g) and a high rapid adsorption rate for a typical organic dye, Rhodamine B (RhB). This could be ascribed to the increased interlayer spacing, the increased specific surface area, and the optimized OH/Fe ratio after the synthetic modification of the pristine BT. The adsorption behavior of RhB onto S-Fe-BT was well described by the pseudo-second-order kinetic model, indicating a chemical-adsorption-controlled process. Furthermore, its adsorption isotherm matched well with the Langmuir model due to a monolayer adsorption process. This paper opens a promising direction to remove the dye pollution using low cost bentonite adsorbents treated by such a convenient modification strategy.

Key words | acid activation, adsorption, bentonite, hydroxyl iron pillaring, Rhodamine B, synergistic modification

HIGHLIGHTS

- Synergistic modification of bentonite by acid activation and hydroxyl iron pillaring was conducted.
- Larger specific surface area and pore volume was achieved after modification.
- Enhanced removal of RhB was achieved by the modified bentonite.
- The adsorption mechanisms of RhB on the adsorbent involve electrostatic attraction and hydrogen bond action.

Huan Xi
Qingqing Li
Jianfeng Zhang (corresponding author)
College of Mechanics and Materials,
Hohai University,
Nanjing 211100, China
E-mail: *jfzhang@hhu.edu.cn*;
jfzhang_sic@163.com

Huan Xi
Yan Yang
Feng Guo
Xiaogang Wang
Shikai Xu
Shiping Ruan
Nanjing Hydraulic Research Institute,
Nanjing 211100, China

Jianfeng Zhang
Jiangsu Engineering Research Center on Utilization of Alternative Water Resources,
Hohai University,
Nanjing 211100, China

Yan Yang
Feng Guo
Desalination and Alternative Water Development & Utilization Research Center,
Hohai University,
Nanjing 211100, China

doi: 10.2166/wst.2020.239

GRAPHICAL ABSTRACT

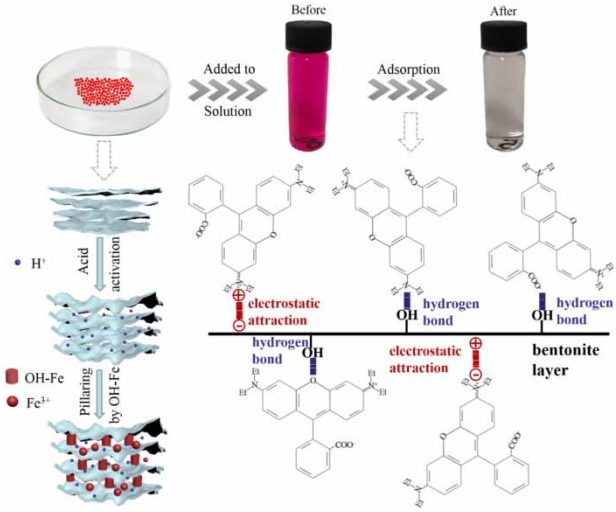

INTRODUCTION

Nowadays, dyes are widely used in many fields, such as textile, paper, plastic, leather, guest-host liquid crystal displays, solar cells, food and mineral processing industries. However, the excessive discharge of dyes will hinder the photo penetration of water, inhibit the photosynthesis of aquatic plants, the growth of biota, and thus destroy the ecological balance (Han *et al.* 2009). Furthermore, many non-biodegradable dyes in water will be harmful to human health and even cause damage to central nervous and reproductive systems due to their high toxicity and bioaccumulation. For example, the typical dye rhodamine B (RhB) is well known as a food additive and sometimes fluorescent water tracer, but its large harmful effects on the human body and ecosystems have forced people to use it with care (Marnani & Shahbazi 2019).

Some methods have already been developed for removing dyes, including precipitation, flocculation, coagulation, incineration, ion exchange, biological degradation and adsorption (Singh *et al.* 2018). Among them, adsorption is very competitive for separating pollutants from water bodies with the advantages of easy operation, relatively low cost and recyclability. Bentonite has been considered to be a promising adsorbent because of its lamellar structure, high cation exchange capacity, and low price with resource abundance (Pereira *et al.* 2017). Many researchers have tried to modify bentonite to enhance the adsorption capacity for cationic dyes (Selvam *et al.* 2008; Farhan *et al.* 2014). For example, Javed *et al.* (2018) prepared activated bentonite using different organic and inorganic acids and conducted batch experiments to investigate its adsorption removal efficiency for Mordant Red 73. The results show that acid activation leached out the Ca^{2+} and Mg^{2+} ions and increased the porosity of bentonite, thus elevating the adsorption capacity to 149 mg/g. Chinoune *et al.* (2016) prepared $Mg(OH)_2$ coated bentonite and found it is efficient for adsorption treatment of reactive blue 2 and reactive blue 19. The iron-pillared bentonite was also prepared by ion exchange using natural bentonite, with which the adsorption capacity of 98.6 mg/g for RhB was obtained.

In this paper, a new facile modification strategy to enhance the adsorption performance of bentonite utilizing synergistic acid activation and hydroxyl iron pillaring was conducted. Herein, different adsorbents were obtained by various combinations of the modification methods, whose adsorption capacities were investigated and compared for a typical organic dye, RhB. To explore the adsorption mechanism of these adsorbents for RhB, the kinetic models and adsorption isotherms were also simulated. Overall, the enhanced adsorption capacity of the modified adsorbents for RhB was validated, suggesting the present strategy is promising for structural modification of dye adsorbents.

MATERIALS AND METHODS

Pristine bentonite and chemicals

The pristine sodium BT powder was obtained from the Hebei Lingshou Dehang Mine products Co., Ltd, China. All the reagent grade chemicals, such as RhB, H_2SO_4, $Fe(NO_3)\cdot 9H_2O$ and Na_2CO_3, were purchased from Sinopharm Chemical Reagent Co. Ltd, China, and used without any further purification.

Preparation of modified BT

(a) Sulphuric acid activation

Herein, 8 g BT powder was added into 50 mL H_2SO_4 solution with a concentration of 1 mol/L, and stirred at a speed of 200 rpm for 24 hours. After that, the mixture was centrifuged at a speed of 8,000 rpm for 8 min and washed with distilled water until the pH reached 6–7. Finally, the mixture was dried in an oven at 60 °C for 12 hours and passed through a 200-mesh sieve to obtain the final powder, labelled as S-BT.

(b) Hydroxyl iron pillaring

24.2 g $Fe(NO_3)_3\cdot 9H_2O$ (0.06 mol) was dissolved in 150 mL distilled water, stirred at room temperature for 1 hour, and then Na_2CO_3 powder was slowly added into the solution. The hydroxyl iron ($Fe(OH)_3$) precipitates as shown in Equation (1).

$$Fe(NO_3)_3 + 1.5xNa_2CO_3 + 1.5xH_2O \rightarrow (1-x)Fe(NO_3)_3 + xFe(OH)_3 + 3xNaNO_3 + 1.5xCO_2 \quad (1)$$

The mixture was stirred for 2 hours at room temperature and aged in a water bath at a temperature of 60 °C for 24 hours. By adjusting the amount of Na_2CO_3, iron pillaring liquid with different ratios of OH^- to Fe^{3+}(OH/Fe) was obtained.

The BT or S-BT powder, 6 g in weight, was stirred at 200 rpm in distilled water at 60 °C for 24 hours, and poured into the hydroxyl iron pillaring liquid, in which the molar ratio of Fe to bentonite was fixed at 100 mmol/g. This mixed solution was also stirred at 200 rpm and 60 °C for 2 hours, and aged for 24 hours at room temperature. The supernatant was centrifuged at 8,000 rpm for 8 min and washed with distilled water three times. Finally, the modified bentonite was dried at 60 °C for 12 hours, ground and passed through a 200-mesh sieve.

(c) Various combinations of sulphuric acid activation and hydroxyl iron pillaring

For comparison, different adsorbents were also obtained by combining and adjusting the modification order of sulphuric acid activation and hydroxyl iron pillaring. For convenience, the abbreviations for the adsorbents used in this study are listed as follows. Schematic illustration for the fabrication process of S-Fe-BT is shown in Figure 1.

BT: Pristine bentonite

S-BT: Sulphuric acid-activated BT

Fe-BT: Hydroxyl iron pillared BT

Fe-S-BT: (a) Sulphuric acid activation + (b) hydroxyl iron pillaring for BT

S-Fe-BT: (b) Hydroxyl iron pillaring + (a) sulphuric acid activation for BT

Microstructural characterization

The X-ray diffraction patterns (XRD) analysis was conducted using a Rigaku 2000 automated diffractometer with CuKα radiation from 5° to 90° at a rate of 5° min^{-1}. Fourier transform infrared (FTIR) spectra were taken on a Nexus 410 spectrometer (Nicolet, USA) and scanned in the wavelength range of 4,000–400 cm^{-1}. The microstructural morphologies were observed by field emission scanning electron microscopy (FESEM, JSM-7600F, JEOL Ltd, Japan). Specific surface area was determined by using the Brunauer-Emmett-Teller (BET) apparatus (Quantachrome Noca Win, USA). The thermogravimetric (TG) analysis was conducted by a STA449C apparatus (Netzsch, Germany) from room temperature to 800 °C at a rate of 10 °C min^{-1} in a nitrogen atmosphere.

RhB adsorption experiments

The adsorption experiments were carried out by a batch method with various RhB concentrations, adsorbent dosages, temperatures and pH. The experiment was performed in 250 mL glass flasks, in which 200 mL RhB solution of different concentrations and 0.2 g adsorbent were added. The solution in the glass flask was agitated by a stirring rod at room temperature at 200 rpm for 5 hours to reach adsorption equilibrium. To explore the effect of initial pH value, 1 mol/L NaOH or 1 mol/L HCl was

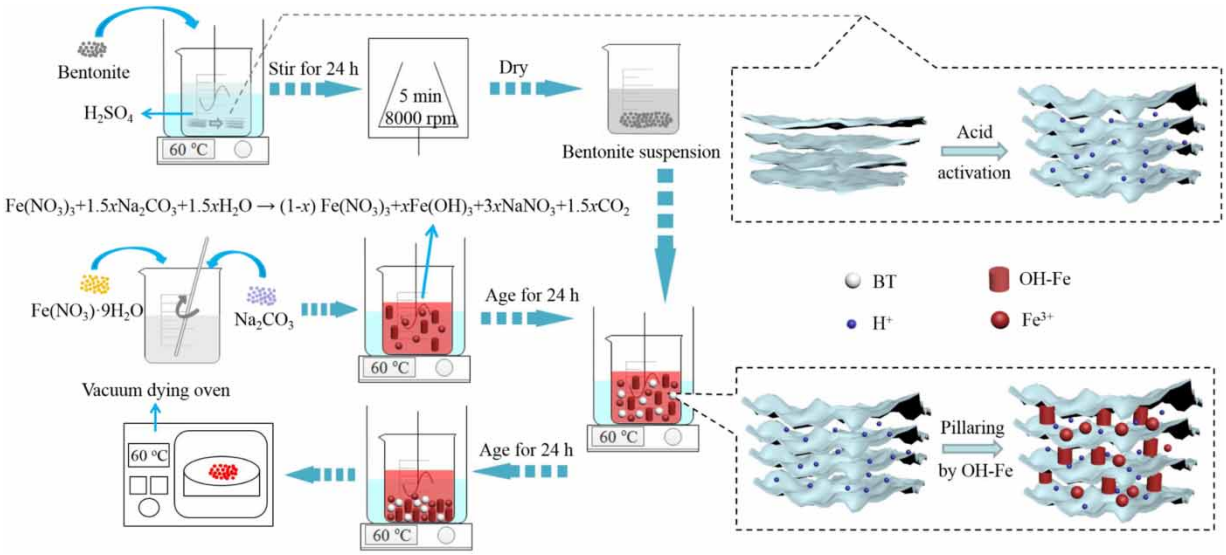

Figure 1 | Schematic illustration for the fabrication process of S-Fe-BT.

added into the solution in order to reach the initial expected pH.

At pre-determined time intervals, the used adsorbents were removed from the solution by centrifugation. Then the RhB concentration in the solution was determined by measuring the absorbance of the solution at 554 nm (λ_{max} for RhB), using a TU1901 UV-Vis spectrophotometer (Purkinje General Instrument Co. Ltd, China). Batch experiments were conducted in triplicate to ensure repeatability and the average values are presented here.

The adsorption amount at time t (q_t), the equilibrium adsorption amount (q_e), and the color removal ratio were measured based on the equations below:

$$q_e = \frac{(C_0 - C_e)V}{W} \tag{2}$$

$$q_t = \frac{(C_0 - C_t)V}{W} \tag{3}$$

$$\text{Color removal}(\%) = \frac{(C_0 - C_t)}{C_0} \times 100\% \tag{4}$$

where C_0 (mg/L), C_e (mg/L) and C_t (mg/L) represent the initial, equilibrium time and t time concentration. V (L) represents the volume of the solution, and W (g) is the weight of the adsorbent powder.

To determine the interactive behavior between the adsorbent and the adsorbate, the adsorption kinetics and isotherm curves were also fitted for investigation, whose detailed experimental procedure and related models can be found in the Supplementary information file.

RESULTS AND DISCUSSION

Analysis of microstructural characterization

The XRD spectra (Figure 2(a)) show that the pristine BT is mainly composed of montmorillonite, quartz and feldspar (Li *et al.* 2015). After modification, the (001) peaks of montmorillonite were found to apparently shift lower, and the d(001) spacing value of S-BT, Fe-BT, S-Fe-BT and Fe-S-BT was calculated to be 1.484 nm, 1.506 nm, 1.543 nm and 1.543 nm, respectively, all higher than that of BT (1.406 nm), indicating the hydroxyl iron was successfully intercalated into the BT layer. More importantly, FTIR spectra were employed to further confirm the structural differences of the BT and S-Fe-BT (Figure 2(b)). Comparing the two spectra of the modified bentonite and pristine bentonite, they showed almost the same peak shape, which indicated that the basic skeleton of bentonite had no obvious change during the modification process. The absorption bands at 3,460 cm^{-1} (H-O-H stretching) and 1,638 cm^{-1} (H-O-H bending) can be ascribed to the water molecules (Hou *et al.* 2011; Wu *et al.* 2014). The three absorption bands at 1,034, 793 and 518 cm^{-1} belong to Si-O stretching vibrations (Hajjaji & El Arfaoui 2009). The characteristic band at 1,383 cm^{-1} reveals the existence of NO_3^- due to the adoption of $Fe(NO_3)_3$ (Hou *et al.* 2011).

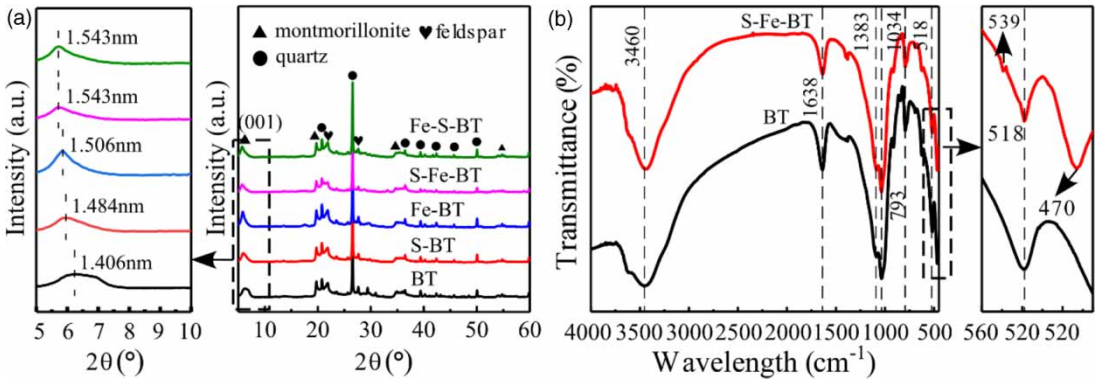

Figure 2 | (a) X-ray diffraction patterns; (b) FTIR spectra of pristine BT and modified BT.

Two small new peaks were observed after the modification of bentonite at 539 cm^{-1} and 470 cm^{-1}, which correspond to the vibration of Si-O-Fe and Fe-O bonds (Nie *et al.* 2009). The change of the spectrum after modification proved that Fe-OH molecules were inserted into the bentonite layers, which is important for RhB adsorption.

Figure 3 shows the N_2 adsorption-desorption isotherm plots for (a) BT and (c) S-Fe-BT, and the corresponding pore size distribution plots ((b) for BT and (d) for S-Fe-BT). The type IV isotherms are observed with apparent hysteresis loops in the P/Po range of 0.4–1.0, indicating the presence of mesopores (Liu *et al.* 2014). The BET specific surface area and total pore volume of S-Fe-BT are both higher than those of BT. In addition, it should also be noticed that the synthetic modification treatment also increased the average pore size. Such a microstructural altering is therefore beneficial for enhanced adsorption performance of BT, which will be validated in the following adsorption testing results (Randelović *et al.* 2014).

The TG-DSC curves of BT and S-Fe-BT are shown in Figure S1(a) and S1(b) (Supplementary information). The first endothermic peak of BT is 112.6 °C, which is attributed to the dehydration of bentonite. The first and second endothermic peaks of S-Fe-BT are 94.3 °C and 130.3 °C, which is attributed to the loss of surface water and interlaminar water of bentonite (Chinoune *et al.* 2016), and the first

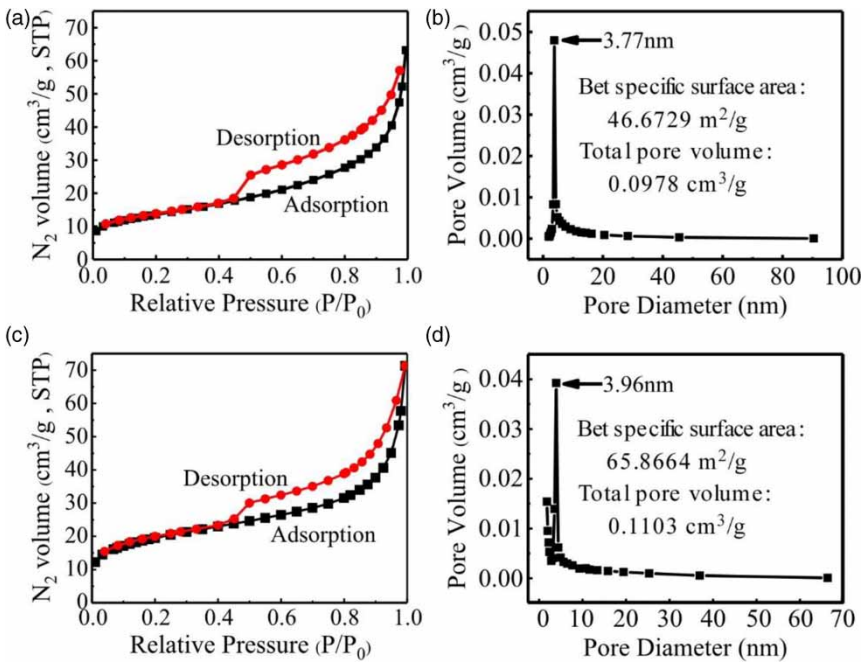

Figure 3 | N_2 adsorption-desorption isotherm and pore size distribution plots of (a), (b) BT; (c), (d) S-Fe-BT.

stage weight loss of BT and S-Fe-BT is determined to be 2.54% and 6.59% respectively. The second endothermic peak at 681.3 °C, with a weight loss of 4.36%, is ascribed to the dehydroxyl reaction of aluminum silicate in BT. However, this completely disappeared for S-Fe-BT due to the enhanced thermal stability after modification.

Figure 4 shows the SEM images of (a) BT, (b) S-BT, (c) Fe-BT, (d) S-Fe-BT and (e) Fe-S-BT, respectively. The pristine BT exhibits a lamellar microstructure with a rough and uneven surface (Figure 4(a)). After acid activation, the pores of BT grow larger and the surface turns smooth (Figure 4(b)). Due to hydroxyl iron intercalation, the spacing of the BT layer (montmorillonite) increases obviously, and the layered structure shows curly morphology (Figure 4(c)).

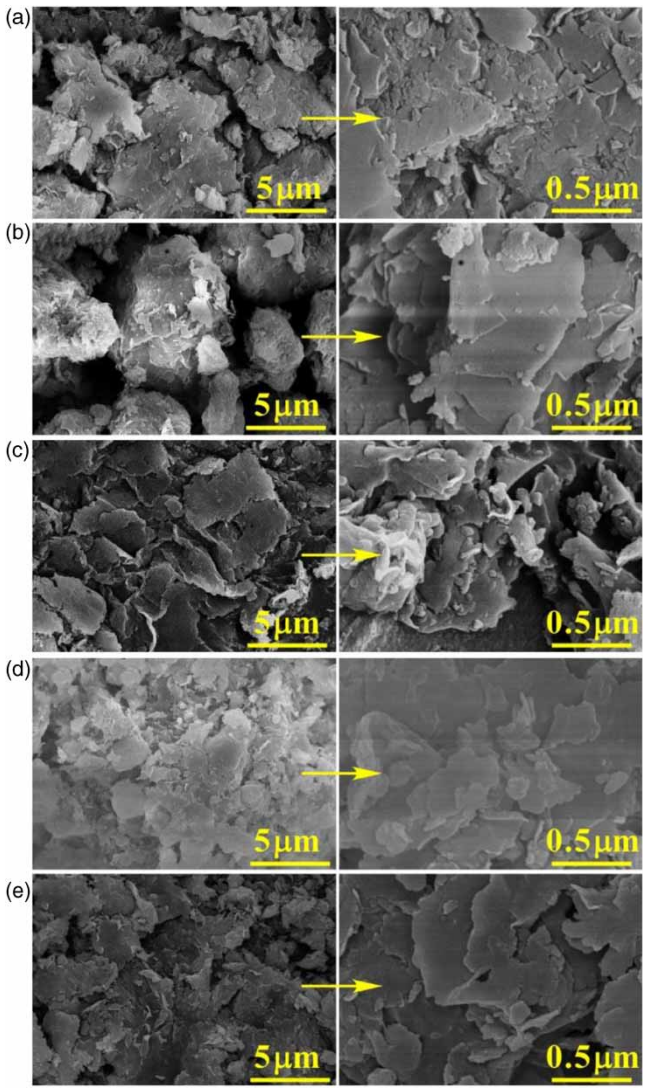

Figure 4 | SEM images of (a) BT; (b) S-BT; (c) Fe-BT; (d) S-Fe-BT; (e) Fe-S-BT.

After the synthetic acid activation and Fe intercalation, some of the lamellae of bentonite peel off, and the pores increase obviously (Figure 4(d) and 4(e)). The OH-Fe particles are well dispersed on the surface of the bentonite with no agglomeration. The mapping of S-Fe-BT is supplied in Figure S2, indicating that the Fe ions are uniformly intercalated into the interlayers of BT. Furthermore, the element contents of BT and S-Fe-BT is also shown in the table embedded in Figure S2(f), where the Fe element was identified due to the successful intercalation of the Fe ion into the bentonite interlayer.

Adsorption of RhB

To investigate the effect of OH/Fe on the adsorption capacity of Fe-BT, RhB solutions (200 mL) with different concentrations of 50 and 100 mg/L were prepared, in which 0.2 g Fe-BT powders were used for adsorption tests. Figure 5(a) and 5(c) indicate that the initial adsorption process happened very fast, and slowed down after 10 hours. Figure 5(b) shows the final removal efficiency of RhB reached higher than 99% for all the Fe-BT powders with a ratio of OH/Fe from 0.05 to 1.0 when the RhB concentration was 50 mg/L. However, when the RhB concentration increased to 100 mg/L (Figure 5(d)), the highest removal efficiency of only 95.7% was obtained at a molar ratio of 0.2 for OH/Fe. A molar ratio less than 0.2 leads to insufficient active adsorption sites, while more than 0.2 results in sites stacking and decreasing removal efficiency.

To compare with adsorption capacity of modified BT with pristine BT, 200 mL RhB solution was prepared with different concentrations from 50 to 300 mg/L, after which 0.2 g adsorbent was added to test the adsorption effect, as shown in Figure 6(a). The adsorption capacity of the pristine BT for RhB was very limited and the removal efficiency was less than 30%. Compared with BT, the adsorption capacity of four modified BT adsorbents was apparently enhanced. When the RhB concentration was 50 mg/L, the removal efficiencies of the four kinds of modified bentonite were all close to 100%. With increasing RhB concentration, the adsorption capacity of these adsorbents decreased, whereas the S-Fe-BT exhibited the highest value. Its adsorption capacity increased from 99.6 mg/g to 246.1 mg/g, after which it declined to 237.8 mg/g with the initial concentration of RhB increased from 100 to 600 mg/L, while the RhB removal efficiency declined from 99.6% to 39.6% due to the saturated active adsorption sites (Figure 6(b)).

To go further, the effects of some typical experimental parameters on RhB removal by S-Fe-BT were investigated.

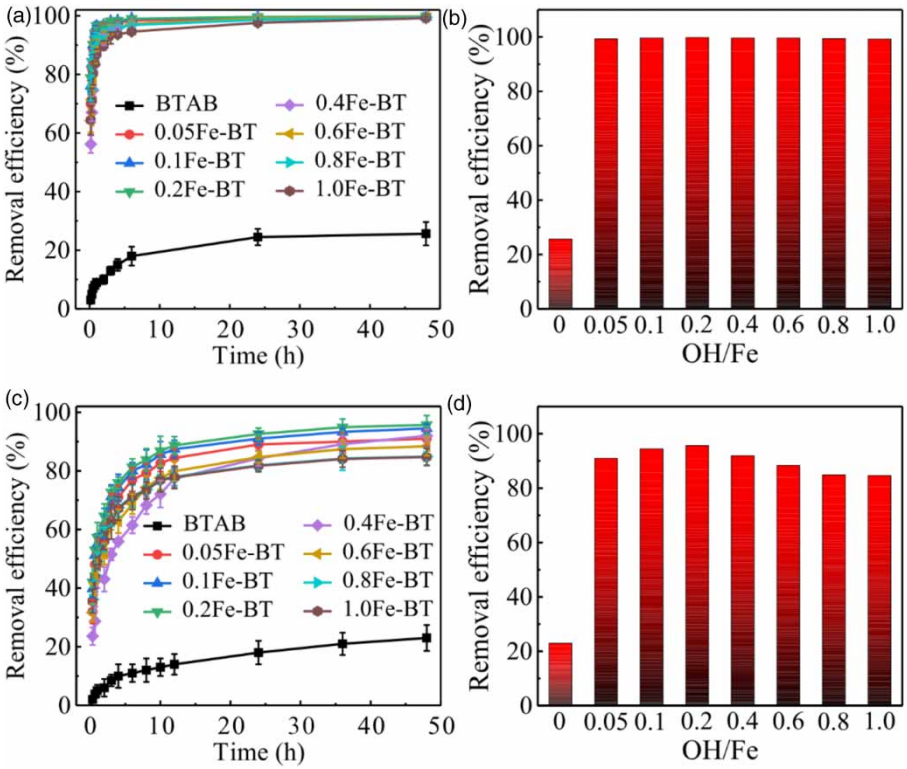

Figure 5 | The effect of adsorption time and OH/Fe on the removal efficiency of RhB by Fe-BT. (a), (b) 50 mg/L RhB; (c), (d) 100 mg/L RhB.

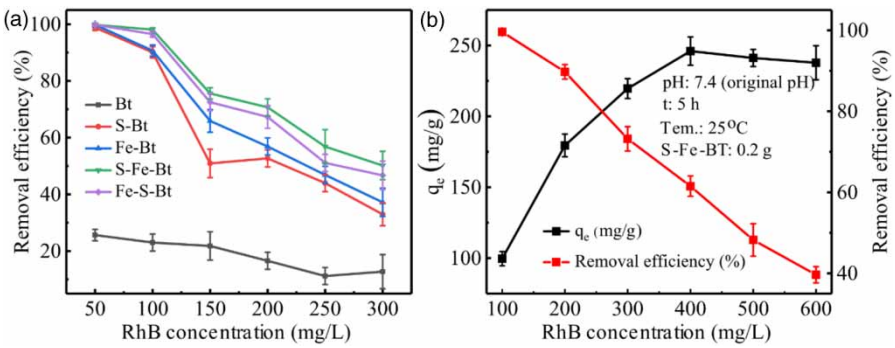

Figure 6 | (a) Removal efficiency of different concentrations of RhB adsorbed by pristine BT and modified BTs; (b) the dependence of adsorption capacity and removal efficiency of S-Fe-BT on RhB concentration.

With increasing S-Fe-BT dosage from 0.025 to 0.2 g, an initial rapid increase in color removal from 14.98% to 99.20% was detected (Figure 7(a)), which may also be ascribed to the availability of more adsorption sites. As the adsorbent dosage increased further (>0.2 g), the color removal remained almost the same, indicating the splitting effect of flux (concentration gradient) occurred between the adsorbent and RhB (Zhang *et al.* 2012). Figure 7(b) shows the effect of adsorption time on the removal efficiency of RhB at 200 mg/L. At the first hour, the color removal increased sharply, after which it gradually slowed down, and approached equilibrium at about 3 hours due to the slow intraparticle diffusion into the interlayer of S-Fe-BT. After 3 hours, a dynamic equilibrium was reached between the adsorption and desorption of the dye.

Figure 7(c) shows that the removal of RhB dye increased with decreasing pH value. As shown in Figure S3 of the Supplementary information file, RhB is a kind of xanthene dye with three forms of protonated species with different charges (Hou *et al.* 2011) of zwitterion

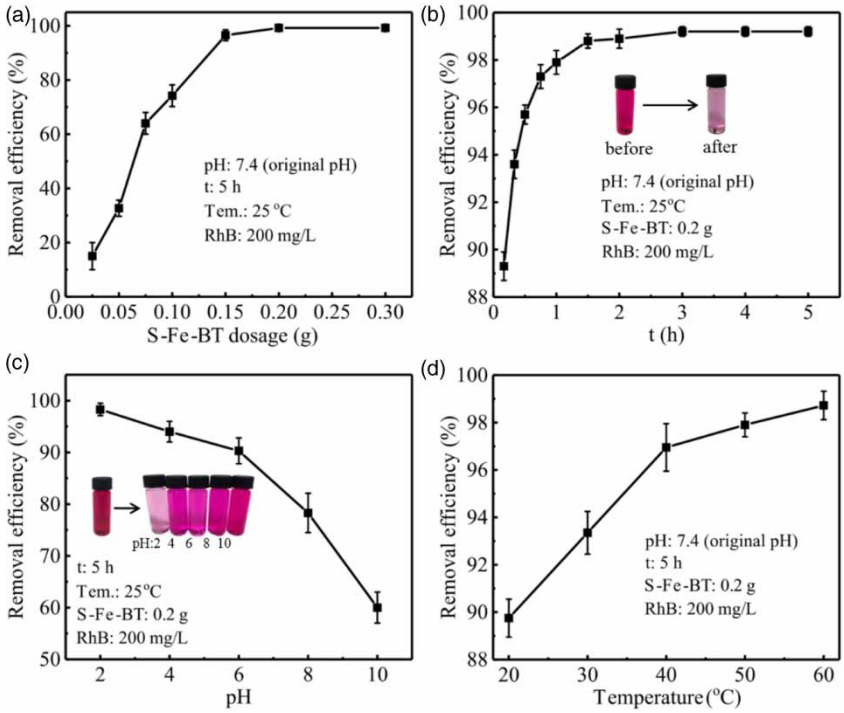

Figure 7 | Effect of some typical experimental parameters on RhB removal efficiency by S-Fe-BT: (a) S-Fe-BT dosage; (b) adsorption time; (c) pH value; (d) adsorption temperature.

($RhB^{\pm}$) and two positively charged species: $RhBH^{+}$ and $RhBH_2^{2+}$. Below pH 3.5, RhB molecules can easily go into adsorbent pores because of its monomeric form. Above pH 3.5, however, RhB in water becomes its zwitterionic form, which is easily aggregated to larger molecules. Therefore, the transport of the molecule inside the pores was hindered, thus reducing the adsorption capacity of the adsorbent. The basic form and lactone form of RhB are predominant in the solution at higher pH values, unfavorable for their adsorption onto adsorbents. In view of the actual situation of the printing and dyeing wastewater and the prevention of acid pollution of the water body, the subsequent experiment still used the neutral dye solution.

With increasing temperature from 20 to 60 °C, the color removal ratio also increased from 89.8% to 98.7% (Figure 7(d)). At lower temperature, the decrease of adsorption capacity may be due to the weakening of the physical interaction between dyes and adsorbents. Since there is only a slight change in the color removal with temperature, it is more practicable to adsorb the dye at room temperature, indicating that the as-obtained S-Fe-BT adsorbent is promising for practical applications.

So far, there are many adsorbents for adsorption of RhB as listed in Table 1. It can be seen that the adsorption capacity of mineral materials is less than 50 mg/g (Khan *et al.* 2012; Bhattacharyya *et al.* 2014; Cai *et al.* 2014). The fabrication of waste-based adsorbents is beneficial for secondary resource utilization, but their adsorption capacity still needs to be improved (Kadirvelu *et al.* 2005; Sureshkumar & Namasivayam 2008). New adsorption materials, such as nanomaterials (Qin *et al.* 2018; Thi Phuong Minh *et al.* 2019) and polymer materials (Huang *et al.* 2008; Wang *et al.* 2015; Saleh & Islam 2018), have received extensive attention. Bentonite with different modifications has also been investigated (Selvam *et al.* 2008; Hou *et al.* 2011). Obviously, in comparison with those reported adsorbents in literature of RhB, the S-Fe-BT adsorbent as a low cost and rapid adsorbent shows comparable adsorption capacity, which is desirable for the treatment and purification of wastewater samples containing similar organic dye.

Adsorption isotherms and kinetics

To determine the interactive behavior between the adsorbent and the adsorbate, we analyzed adsorption isotherm models, including the Langmuir, Freundlich and Temkin models (Supplementary information S1).

As can be seen from Figure S4 and Table S1, the regression coefficient (R^2) of RhB adsorption isotherms on to S-Fe-BT obtained from the Langmuir isotherm under

Table 1 | Adsorption capacity of RhB dyes by different adsorbents

Rough classification	No.	Adsorbents	Adsorption conditions (initial concentration, pH and temperature)	Adsorption capacity (mg/g)	Removal (%)	Reference
Mineral	1	Pyrite	10 mg/L; pH:4.0; 25 °C	21.3	/	Cai *et al.* (2014)
	2	Acid-treated kaolinite	350 mg/L; pH:7.0; 20 °C	23.7	/	Bhattacharyya *et al.* (2014)
	3	Kaolinite	90 mg/L; pH:7.0; 30 °C	46.1	83	Khan *et al.* (2012)
Waste-based	4	Sago waste activated carbon	10 mg/L; pH:5.7; 25 °C	16.1	100	Kadirvelu *et al.* (2005)
	5	Surfactant-modified coconut coir pith	20 mg/L; pH:7.0; 25 °C	14.9	97	Sureshkumar & Namasivayam (2008)
Nanoparticles	6	SDS-modified alumina nanoparticles	10^{-4} mol/L; pH:4.0; 25 °C	165.0	97.7	Thi Phuong Minh *et al.* (2019)
	7	Monodispersed mesoporous silica nanoparticles	10 mg/L; pH:7.0; 25 °C	23.2	96	Qin *et al.* (2018)
Polymer	8	Polyamide grafted carbon microspheres	$2*10^{-6}$ mol/L; pH:10.0; 25 °C	19.9	100	Saleh & Islam (2018)
	9	Polymeric nanotubes	100 mg/L; pH:7.0; 25 °C	35.6	99	Wang *et al.* (2015)
	10	Hypercrosslinked polymeric adsorbent	100–600 mg/L; pH:7.0; 20 °C	25.0–55.0	97	Huang *et al.* (2008)
Bentonite	11	Acid-treated montmorillonite	400 mg/L; pH:7.0; 20 °C	188.7	/	Bhattacharyya *et al.* (2014)
	12	Fe-bentonite	320 mg/L; pH:3.0; 25 °C	98.6	/	Hou *et al.* (2011)
	13	Sodium montmorillonite	300 mg/L; pH:7.0; 30 °C	42.2	/	Selvam *et al.* (2008)
	14	S-Fe-BT	300 mg/L; pH:7.0; 25 °C	246.1	100	This work

different temperatures is higher ($R^2 = 0.9834$, 0.7729 and 0.8720, respectively) than those from the Freundlich and Temkin isotherms, while the root mean square (RMS) is lower. This indicates that the Langmuir isotherm is a better fit and that adsorption phenomenon is in monolayer. The separation factor (R_L) values are 0.0030–0.0750 for S-Fe-BT, suggesting that the adsorption of RhB on S-Fe-BT is a favorable adsorption process (Muinde *et al.* 2017; Venkatesan & Narayanan 2018).

In order to understand the mechanism of the adsorption kinetic process, the experimental data were fitted by the following three kinetic models (Supplementary information S2), and the results are shown in Figure S5. Tables S2 and S3 summarize the pseudo-first-order (Figure S5(a) and S5(b)), pseudo-second-order (Figure S5(c) and S5(d)) and intraparticle diffusion kinetics (Figure S5(e) and S5(f)) constants obtained from a linear regression analysis. For the pseudo-second-order kinetics model, high correlation coefficients ($R^2 >$ 0.999) were obtained with low RMS (<0.0002) for all RhB concentrations and temperatures. It is well known that the pseudo second model is based on the rate control step of chemical reaction or chemisorption through electron sharing or electron gain and loss, so we consider that the adsorption process was primarily controlled by chemisorption. Moreover, the experimental data matched well with the theoretical q_e values, indicating that this adsorption process conformed to pseudo-second-order kinetics. When the initial RhB concentration increased, the q_e values increased while the rate constants (k_2) decreased. This could be attributed to the relationship between the competition of adsorption sites and RhB concentration. At lower concentrations, less competition occurred for the sorption surface sites, while at higher concentrations, the competition for the active sites between RhB molecules was high, and consequently lower k_2 values were obtained. The rise of temperature was accompanied by the rise of k_2, indicating that the reaction rate was accelerated at higher temperatures.

The Weber intraparticle diffusion model was also employed to identify the steps that occurred during the adsorption process. The linear plots of various initial concentrations did not pass through the origin point (Figure S5(e) and S5(f)), suggesting that the adsorption rate was not controlled by intraparticle diffusion. The intercept value, C, was used to represent the thickness of the boundary layer and played a significant role in the removal of the dye. Generally, the larger the C value is, the more significant the boundary layer effect is. The C values increased from 84.6 to 134.2 mg/g with increasing initial dye

concentration from 100 to 250 mg/L (Table S3), suggesting a boundary layer diffusion effect. From above, it can be concluded that pseudo-second-order and intraparticle diffusion took place simultaneously, which effectively enhanced the adsorption capacity of S-Fe-BT.

Adsorption mechanism

As a cationic dye, the RhB molecules are positively charged in neutral and alkaline solution, which can produce electrostatic attraction with the negatively charged bentonite layer. However, the protons on the hydroxyl groups of RhB molecules can be ionized under acidic conditions, which leads the dye molecules to be negatively charged and cause electrostatic attraction with the Fe^{3+} of S-Fe-BT. Furthermore, the adsorption isotherms fitted the Langmuir model, indicating that electrostatic attraction is not the dominant mechanism of adsorption. Besides, hydrogen bonding interaction may occur between RhB and S-Fe-BT (Deng *et al.* 2019). In more detail, the hydrogen bonding interaction may happen between the hydroxyl group of S-Fe-BT and the oxygen of the xanthenes ring as well as the aromatic ring of RhB molecule (Mohammadi *et al.* 2010). The interaction could also occur between the hydroxyl groups from the adsorbed H_2O in the interlayer of S-Fe-BT and all of the N and O atoms in the RhB molecule (Yu *et al.* 2013). In summary, as shown in Figure 8, the adsorption mechanisms of RhB on the surface of the adsorbent are chemical adsorption through hydrogen bond action with monolayer and uniform active sites as well as physical adsorption through electrostatic attraction (De Castro *et al.* 2018; de Queiroga *et al.* 2019).

CONCLUSIONS

In this paper, a facile modification strategy for BT was proposed by synergistic acid activation and hydroxyl iron pillaring, after which the interlayer spacing was enlarged with increased BET specific surface area and total pore volume. The maximum adsorption capacity of S-Fe-BT was found to be 246.06 mg/g without pH adjustment when the RhB concentration was 400 mg/L. The equilibrium adsorption isotherm followed the Langmuir model better than the Freundlich or Temkin model, suggesting that the adsorption phenomenon is monolayer and the adsorption sites of adsorbents are uniform. The experimental data fits well with the pseudo-second-order adsorption model

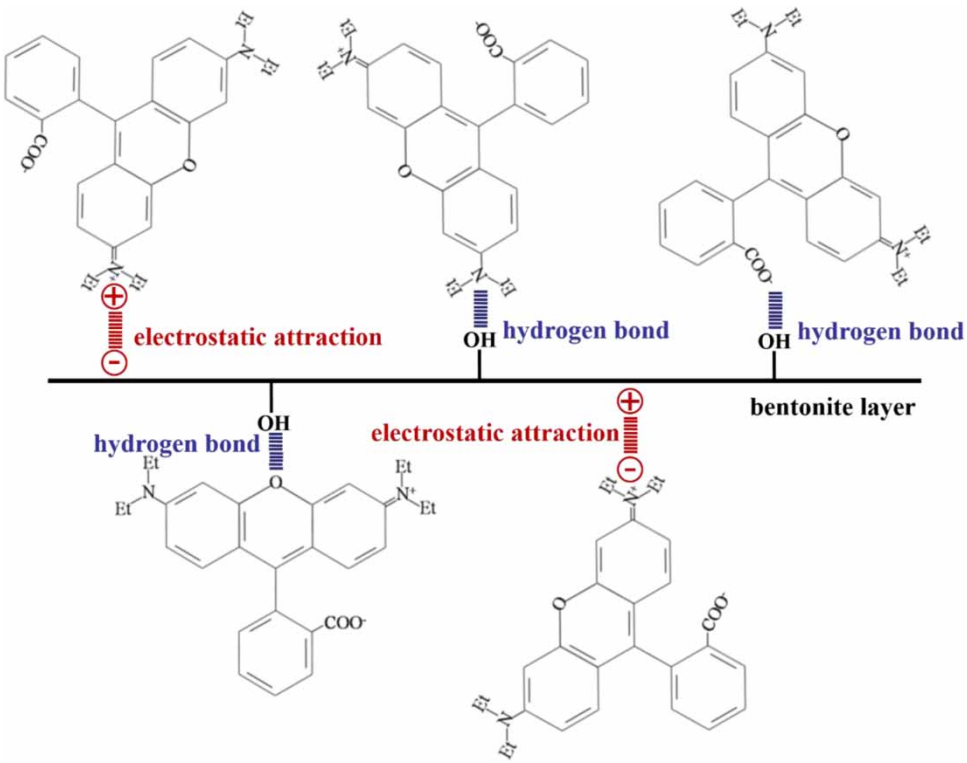

Figure 8 | Proposed adsorption mechanism of S-Fe-BT for the basic form of RhB.

($R_2^2 = 0.9999$), indicating that the adsorption was controlled by a chemical process. Adsorption mechanisms of RhB on S-Fe-BT were electrostatic attraction and formation of hydrogen bonds. Therefore, the modified BT obtained in this study is highly proposed as a promising adsorbent for the removal of RhB from water environments.

ACKNOWLEDGEMENTS

The authors would like to acknowledge the financial supports from National Key R&D Program of China (2018YFC0408003,2018YFC1508704).

SUPPLEMENTARY MATERIAL

The Supplementary Material for this paper is available online at https://dx.doi.org/10.2166/wst.2020.239.

REFERENCES

Bhattacharyya, K. G., SenGupta, S. & Sarma, G. K. 2014 Interactions of the dye, Rhodamine B with kaolinite and montmorillonite in water. *Applied Clay Science* **99**, 7–17.

Cai, K., Xiong, S. W., Zhang, X. X., Rui-Ping, L. I. & Huang, Y. P. 2014 Adsorption characteristics of cationic organic dye RhB on pyrite. *Acta Petrologica Et Mineralogica* **33** (2), 370–376.

Chinoune, K., Bentaleb, K., Bouberka, Z., Nadim, A. & Maschke, U. 2016 Adsorption of reactive dyes from aqueous solution by dirty bentonite. *Applied Clay Science* **123**, 64–75.

De Castro, M. L. F. A., Abad, M. L. B., Sumalinog, D. A. G., Abarca, R. R. M., Paoprasert, P. & de Luna, M. D. G. 2018 Adsorption of methylene blue dye and Cu (II) ions on EDTA-modified bentonite: isotherm, kinetic and thermodynamic studies. *Sustainable Environment Research* **28** (5), 197–205.

Deng, H., Mao, Z., Xu, H., Zhang, L., Zhong, Y. & Sui, X. 2019 Synthesis of fibrous $LaFeO_3$ perovskite oxide for adsorption of Rhodamine B. *Ecotoxicology and Environmental Safety* **168**, 35–44.

de Queiroga, L. N. F., França, D. B., Rodrigues, F., Santos, I. M., Fonseca, M. G. & Jaber, M. 2019 Functionalized bentonites for dye adsorption: depollution and production of new pigments. *Journal of Environmental Chemical Engineering* **7** (5), 103333.

Farhan, A. M., Sameen, A. S., Farhan, A. M. & Sameen, A. S. 2014 Kinetic study of adsorption Rhodamine 6G Dye from aqueous solutions using Bentonite Clay. *American Journal of Environmental Engineering* **4**, 11–17.

Hajjaji, M. & El Arfaoui, H. 2009 Adsorption of methylene blue and zinc ions on raw and acid-activated bentonite from Morocco. *Applied Clay Science* **46** (4), 418–421.

Han, R., Wang, Y., Zhao, X., Wang, Y., Xie, F., Cheng, J. & Tang, M. 2009 Adsorption of methylene blue by phoenix tree leaf powder in a fixed-bed column: experiments and prediction of breakthrough curves. *Desalination* **245** (1–3), 284–297.

Hou, M. F., Ma, C. X., Zhang, W. D., Tang, X. Y., Fan, Y. N. & Wan, H. F. 2011 Removal of Rhodamine B using iron-pillared bentonite. *Journal of Hazardous Materials* **186** (2–3), 1118–1123.

Huang, J. H., Huang, K. L., Liu, S. Q., Wang, A. T. & Yan, C. 2008 Adsorption of Rhodamine B and methyl orange on a hypercrosslinked polymeric adsorbent in aqueous solution. *Colloids & Surfaces A Physicochemical & Engineering Aspects* **330** (1), 55–61.

Javed, S. H., Zahir, A., Khan, A., Afzal, S. & Mansha, M. 2018 Adsorption of mordant Red 73 dye on acid activated bentonite: kinetics and thermodynamic study. *Journal of Molecular Liquids* **254**, 398–405.

Kadirvelu, K., Karthika, C., Vennilamani, N. & Pattabhi, S. 2005 Activated carbon from industrial solid waste as an adsorbent for the removal of Rhodamine-B from aqueous solution: kinetic and equilibrium studies. *Chemosphere* **60** (8), 1009–1017.

Khan, T. A., Dahiya, S. & Ali, I. 2012 Use of kaolinite as adsorbent: equilibrium, dynamics and thermodynamic studies on the adsorption of Rhodamine B from aqueous solution. *Applied Clay Science* **69** (21), 58–66.

Li, J.-s., Xue, Q., Wang, P. & Li, Z.-z. 2015 Effect of lead (II) on the mechanical behavior and microstructure development of a Chinese clay. *Applied Clay Science* **105**, 192–199.

Liu, H., Wei, C., Cheng, L., Liu, Y. U. & Dong, C. 2014 Magnetic mesoporous clay adsorbent: preparation, characterization and adsorption capacity for atrazine. *Microporous & Mesoporous Materials* **194** (7), 72–78.

Marnani, N. & Shahbazi, A. 2019 A novel environmental-friendly nanobiocomposite synthesis by EDTA and chitosan functionalized magnetic graphene oxide for high removal of Rhodamine B: adsorption mechanism and separation property. *Chemosphere* **218**, 715–725.

Mohammadi, M., Hassani, A. J., Mohamed, A. R. & Najafpour, G. D. 2010 Removal of rhodamine B from aqueous solution using palm shell-based activated carbon: adsorption and kinetic studies. *Journal of Chemical & Engineering Data* **55** (12), 5777–5785.

Muinde, V., Onyari, J. M., Wamalwa, B. M. & Wabomba, J. 2017 *Adsorption of Malachite Green From Aqueous Solutions Onto Rice Husks: Kinetic and Equilibrium Studies*.

Nie, J. J., Wang, L. J. & Zhou, H. 2009 Infrared spectroscopic analysis of bentonite from Balikun in Xinjiang. *Rock & Mineral Analysis* **28** (1), 69–71.

Pereira, F. A., Sousa, K. S., Cavalcanti, G. R., França, D. B., Queiroga, L. N., Santos, I. M., Fonseca, M. G. & Jaber, M. 2017 Green biosorbents based on chitosan-montmorillonite beads for anionic dye removal. *Journal of Environmental Chemical Engineering* **5** (4), 3309–3318.

Qin, P., Yang, Y., Zhang, X., Niu, J., Yang, H., Tian, S., Zhu, J. & Lu, M. 2018 Highly efficient, rapid, and simultaneous removal of cationic dyes from aqueous solution using monodispersed

mesoporous silica nanoparticles as the adsorbent. *Nanomaterials* **8** (1), 4.

Ranđelović, M. S., Purenović, M. M., Matović, B. Z., Zarubica, A. R., Momčilović, M. Z. & Purenović, J. M. 2014 Structural, textural and adsorption characteristics of bentonite-based composite. *Microporous & Mesoporous Materials* **195** (195), 67–74.

Saleh, T. A. & Islam, A. 2018 Synthesis of polyamide grafted carbon microspheres for removal of rhodamine B dye and heavy metals. *Journal of Environmental Chemical Engineering* **6** (4), 5361–5368.

Selvam, P. P., Preethi, S., Basakaralingam, P., Thinakaran, N., Sivasamy, A. & Sivanesan, S. 2008 Removal of rhodamine B from aqueous solution by adsorption onto sodium montmorillonite. *Journal of Hazardous Materials* **155** (1–2), 39–44.

Singh, N. B., Nagpal, G., Agrawal, S. & Rachna 2018 Water purification by using adsorbents: a review. *Environmental Technology & Innovation* **11**, 187–240.

Sureshkumar, M. V. & Namasivayam, C. 2008 Adsorption behavior of direct Red 12B and Rhodamine B from water onto surfactant-modified coconut coir pith. *Colloids & Surfaces A Physicochemical & Engineering Aspects* **317** (1–3), 277–283.

Thi Phuong Minh, C., Ngoc Trung, N., Thi Lan, V., Thi Huong, D., Lan Chi, D., Hai Long, N., Thu Ha, H., Thanh Son, L. & Tien Duc, P. 2019 Synthesis, characterization, and modification of alumina nanoparticles for cationic Dye removal. *Materials* **12** (3), 450.

Venkatesan, G. & Narayanan, S. L. 2018 Synthesis of Fe_2O_3-coated and HCl-treated bauxite ore waste for the adsorption of arsenic (III) from aqueous solution: isotherm and kinetic models. *Chemical Engineering Communications* **205** (1), 34–46.

Wang, M., Fu, J., Zhang, Y., Chen, Z., Wang, M., Zhu, J., Cui, W., Zhang, J. & Xu, Q. 2015 Removal of Rhodamine B, a cationic dye from aqueous solution using poly(cyclotriphosphazene-Co-4,4′-sulfonyldiphenol) nanotubes. *Journal of Macromolecular Science: Part A – Chemistry* **52** (2), 105–113.

Wu, L., Tong, D., Zhao, L., Yu, W., Zhou, C. & Wang, H. 2014 Fourier transform infrared spectroscopy analysis for hydrothermal transformation of microcrystalline cellulose on montmorillonite. *Applied Clay Science* **95**, 74–82.

Yu, Y., Murthy, B. N., Shapter, J. G., Constantopoulos, K. T., Voelcker, N. H. & Ellis, A. V. 2013 Benzene carboxylic acid derivatized graphene oxide nanosheets on natural zeolites as effective adsorbents for cationic dye removal. *Journal of Hazardous Materials* **260**, 330–338.

Zhang, J., Zhou, Q. & Ou, L. 2012 Kinetic, isotherm, and thermodynamic studies of the adsorption of methyl orange from aqueous solution by chitosan/alumina composite. *Journal of Chemical & Engineering Data* **57** (2), 412–419.

First received 7 March 2020; accepted in revised form 4 May 2020. Available online 18 May 2020